Explaining Bayesian Neural Networks

Kirill Bykov[*,a,d], Marina M.-C. Höhne[*,⋆,a,d], Adelaida Creosteanu[i], Klaus-Robert Müller[⋆,a,b,c,d,e], Frederick Klauschen[g,h], Shinichi Nakajima[a,d,j], Marius Kloft[⋆,f]

Abstract—To make advanced learning machines such as Deep Neural Networks (DNNs) more transparent in decision making, explainable AI (XAI) aims to provide interpretations of DNNs' predictions. These interpretations are usually given in the form of heatmaps, each one illustrating relevant patterns regarding the prediction for a given instance. Bayesian approaches such as Bayesian Neural Networks (BNNs) so far have a limited form of transparency (*model* transparency) already built-in through their prior weight distribution, but notably, they lack explanations of their predictions for given instances. In this work, we bring together these two perspectives of transparency into a holistic explanation framework for explaining BNNs. Within the Bayesian framework, the network weights follow a probability distribution. Hence, the standard (deterministic) prediction strategy of DNNs extends in BNNs to a predictive distribution, and thus the standard explanation extends to an *explanation distribution*. Exploiting this view, we uncover that BNNs implicitly employ multiple heterogeneous prediction strategies. While some of these are inherited from standard DNNs, others are revealed to us by considering the inherent uncertainty in BNNs. Our quantitative and qualitative experiments on toy/benchmark data and real-world data from pathology show that the proposed approach of explaining BNNs can lead to more effective and insightful explanations.

Index Terms—Explainable AI, Bayesian Neural Networks, Deep Neural Networks, LRP.

I. INTRODUCTION

DEEP Neural Networks (DNNs) have achieved significant success over the years, helping to advance Artificial Intelligence (AI). Driven by the exponential growth in available data and computational resources, DNNs achieve state-of-the-art results across various fields of Machine Learning (ML), such as Computer Vision (CV) [1], [2], [3], Natural Language Processing (NLP) [4], [5], [6], [7], and Reinforcement Learning (RL) [8], [9], [10]. Although current Deep Learning research is still far away from achieving general

*: Equal contribution
⋆: corresponding authors
[a] : Machine Learning Group, Technische Universität Berlin, Marchstr. 23, Berlin 10587, Germany
[b] : Department of Artificial Intelligence, Korea University, Anam-dong, Seongbuk-gu, Seoul 02841, Korea
[c] : Max Planck Institute for Informatics, Stuhlsatzenhausweg 4, Saarbrücken 66123, Germany
[d] : BIFOLD - Berlin Institute for the Foundations of Learning and Data, Technische Universität Berlin, Berlin, Germany
[e] : Google Research, Brain team, Berlin, Germany
[f] : Department of Computer Science - TU Kaiserslautern, Germany
[g] : German Cancer Consortium (DKTK), German Cancer Research Center (DKFZ), Heidelberg, Germany
[h] : Institute of Pathology, Charite – Universitätsmedizin Berlin, Berlin, Germany.
[i] : Aignostics, Berlin, Germany
[j] : RIKEN AIP, 1-4-1 Nihonbashi, Chuo-ku, Tokyo, Japan

Artificial Intelligence [11], there are already specific domains where DNNs could surpass human performance, such as game-playing or image recognition tasks [12], [13], [14], [10]. DNNs accomplish such high performance by learning mappings from raw data to meaningful representations.

With the increasing complexity of modern Neural Networks [15], it is a difficult task to explain what particular features do influence the prediction. Therefore, DNNs have often been considered as 'black-box' [16], [17]. However, especially in security-critical applications (such as autonomous driving or personalized medicine), transparency of the decision-making model is mandatory and therefore the network's inability to explain its predictions restricts the applicability of ML systems. Indeed, despite showing great performance in test environments, DNNs have not yet reached universal acceptance in the above-mentioned areas [18].

Recently, the field of *Explainable AI (XAI)* has emerged to address these concerns (see e.g. [19]). XAI aims to develop and study methodologies for explaining the predictions made by advanced learning machines such as DNNs. Recent advances in XAI have led to a variety of novel methods [20], [21], [22]. These can be grouped into *global* and *local* explanation methods. While global explanation methods interpret the decision making of DNNs across a population (e.g. by visualizing the 'prototypical' cases [23], [24], [25], or by detecting semantic elements [16], [26]), local explanations provide interpretations of the prediction for a particular data example by attributing relevances to the input features [27], [28], [29], [30], [31], [32], [27], [33], [34], [35], [36], [37], [38].

Most of the explanation methods, local and global ones, are developed for DNNs trained in a maximum-a-posteriori (MAP) setting, where the DNN weights are point estimates. In contrast, Bayesian Neural Networks (BNNs) learn a distribution of the network weights, which induces also a distribution on the prediction. For a better intuition on the advantage in explainability of a BNN over a DNN, let us consider the example image shown in Figure 1. Shown on the left is a histopathological image [39], [40] taken from a cancer patient (see e.g. [41], [42], [43]). From this image, smaller patches are extracted and fed into a DNN, trained to classify patches into cancer or non-cancer. In the center of Figure 1, we show the prediction score of a regular (non-Bayesian) DNN for the class *cancer*. While these scores are usually normalized with a softmax function, these scores do not represent actual probabilities [44] — The DNN provides no information on how certain or uncertain the patches' relevances are the prediction. This additional information is provided by BNNs (shown on the right), e.g. in the form of the variances shown
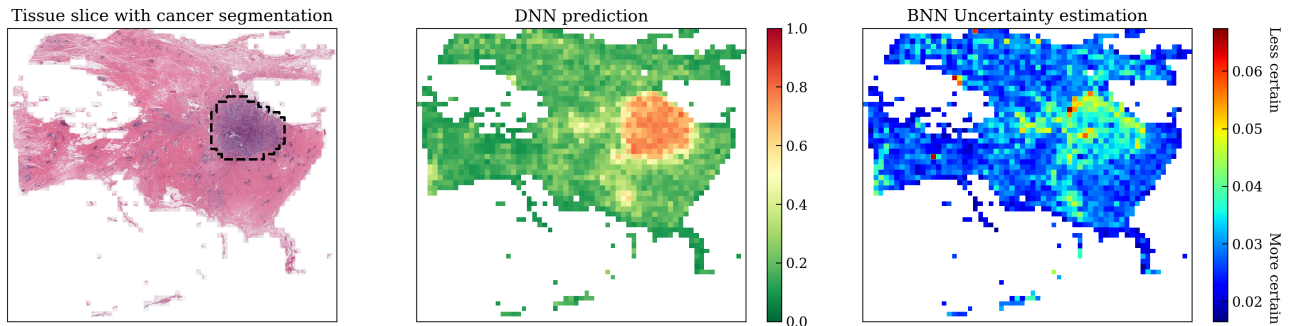
Fig. 1: Illustrating practical benefits of BNNs over regular DNNs. Left: A whole slide image from a cancer patient, divided into smaller patches. Center: The prediction accuracy for the class cancer of a standard DNN (which is identical to the mean prediction of a corresponding BNN using Laplace approximation). Right: Compared with a standard DNN, the BNN gives us additional information, in the form of uncertainties about the respective patch predictions. The Green (red) color here indicates a high (low) level of certainty.

on the right of Figure 1.

We observe that there are distinct regions where the model is significantly more certain about a patch showing cancer cells (highlighted in blue colors) than in other regions (highlighted in green, with red referring to the most uncertain regions).

Thus, the BNN can not only provide predictions but also evaluate their faithfulness. On the other hand, BNNs are—as regular DNNs— black boxes not yielding explanations out of the box (e.g., in the form of heatmaps).

The present work contributes to closing this gap. We provide a method for explaining BNNs. It translates uncertainty information of a BNN into feature relevance uncertainties (in the input space), thus yielding an explanation with error bars (uncertainty heatmaps) or more general quantile heatmaps. Our model is even applicable to regular DNNs (e.g., CNNs) trained in a non-Bayesian fashion, which can first be translated into BNNs (e.g., using MC dropout [45] or Laplace approximation [46], [47]), and then explained using our proposed method. Thus our approach can enrich the explanation of regular DNNs by additional uncertainty information.

To illustrate this advantage, consider again the medical task illustrated in Fig 1. The first step towards transparency of the shown model is assigning the input features with relevance scores; this is what explanation methods of regular DNNs do. It helps to identify the areas in the image that were relevant for the prediction. Our BNN explanation would additionally provide information on regions where the method is confident about the relevance scores. This may enable an expert to faster identify the most significant cancer areas in an image. On the other hand, the expert might want to look specifically into areas of low confidence to resolve this low confidence by contributing with human expert knowledge to cancer image evaluation. Hence, by determining the level of certainty required by a particular case or by visualizing multiple levels of certainty at once in an explanation, our method can lead to additional insight into the underlying prediction strategy of a model.

In this work, we will propose and investigate different techniques for explaining the decision-making process of

(deep) BNNs. Our suggested approaches are method-agnostic, i.e. they can build on any arbitrary explanation method for regular (non-Bayesian) *DNNs*, which is transformed into a local attribution method for *BNNs*. The proposed method can be combined with any (approximate) inference procedure of BNNs. In computational experiments, our approach interestingly revealed that BNNs implicitly employ multiple heterogeneous prediction strategies. The reason is that BNNs exhibit numerous modes, and approximately one can think of a mode as a prototypical prediction strategy. In contrast, in a standard non-Bayesian DNN, the prediction is deterministic and thus cannot extract multi-modal explanations. With our proposed method, we are now able to visualize the different modes thus revealing the intrinsic multi-modality in the decision-making of BNNs (and by association: DNNs). For practical purposes and to enable the reader to replicate our results we publish our source code[1].

In the following we summarize the main contributions of this work:

- We provide a theoretical justification along with a detailed practical explanation for usage of the **Mean Explanation** as the most simplistic option to explain the decision-making process of a BNN.
- We propose a new method called **UAI**: Union and Intersection Explanation—a practical approach that is capable of translating the uncertainty information of a BNN's prediction into input feature uncertainty, thus enriching the XAI explanations with (un)certainty information.
- We investigate the **multi-modality** and variability of the decision-making process of BNNs by clustering sampled explanations.
- **Generality:** We observe that local attribution of regular (non-Bayesian) DNNs can be enhanced by *Bayesianization* procedure: approximating posterior distribution around mode weights.

---

[1]The code will be made available on github.

II. BACKGROUND AND RELATED WORK

This section provides a comprehensive overview of BNNs and well established local explanation methods.

A. Bayesian Neural Networks

From a statistical perspective, standard DNNs are usually trained using *maximum a-posteriori (MAP) optimization* [48]:

$$\hat{W} = \text{argmax}_W \log p(W \mid \mathcal{D}_{\text{tr}}), \tag{1}$$
$$= \text{argmax}_W \log p(\mathcal{D}_{\text{tr}} \mid W) + \log p(W),$$

which reduces to the maximum likelihood estimation when the prior distribution $p(W)$ is flat. The most commonly used loss functions and regularizers fit into this framework, such as categorical cross-entropy for classification or mean squared error for regression. Although this procedure is efficient since the networks only learn a fixed set of weights, it does not provide uncertainty information about the learned weights and subsequently on the prediction. In contrast, Bayesian neural networks (BNNs) estimate the posterior *distribution* of weights, and thus, provide uncertainty information on the prediction, which can provide confidence information on predictions. Particularly, in critical real-world applications of deep learning—for instance, medicine [42], [49], [41] and autonomous driving [50], [51]—where predictions need to be highly precise and wrong predictions could easily be fatal, the availability of prediction uncertainties can be of fundamental advantage.

Let $f_W : \mathbb{R}^d \to \mathbb{R}^k$ be a feed-forward neural network with the weight parameter $W \in \mathcal{W}$. Given a training dataset $\mathcal{D}_{\text{tr}} = \{x_n, y_n\}_{n=1}^N$, Bayesian learning (approximately) learns the posterior distribution

$$p\left(W|\mathcal{D}_{\text{tr}}\right) = \frac{p(\mathcal{D}_{\text{tr}}|W)p(W)}{\int_{\mathcal{W}} p(\mathcal{D}_{\text{tr}}|W)p(W)dW} , \tag{2}$$

where $p(W)$ is the prior distribution of the weight parameter. After training, the output for a given test sample x is predicted by the distribution:

$$p(y|x, \mathcal{D}_{\text{tr}}) = \int_{\mathcal{W}} p(y|f_W(x))p(W|\mathcal{D}_{\text{tr}})dW. \tag{3}$$

Since the denominator of the posterior, shown in Eq. (2), is intractable for neural networks, numerous approximation methods have been proposed, e.g., Laplace approximation [47], Variational Inference [52], [53], MC dropout [54], Variational Dropout [55], [56], MCMC sampling [57], and SWAG [58], [59]. With these approximation methods, one can now efficiently draw samples from the approximate posterior distribution of the network parameters (Eq. (3)), and compute statistics, e.g., mean and variance, of the prediction for a given data point x. Classical MAP training procedures could also be seen as performing approximate Bayesian inference, using the approximate posterior $p(W|\mathcal{D}_{\text{tr}}) \approx \delta(W = \hat{W})$, where δ is the Dirac delta function.

B. Local attribution methods

Local explanation methods attribute *relevance* to the input (features) or intermediate nodes [28], [29], [30], [33] by using a relevance attribution operation, which we define as follows:

Definition 1 (Relevance Attribution operator): An operator $\mathcal{T}_{x,W}[\cdot]$ that maps an output function $f_W : \mathbb{R}^d \to \mathbb{R}^k$ to a relevance function $R : \mathbb{R}^d \to \mathbb{R}^d$ is called a relevance attribution operator:

$$R_W(x) = \mathcal{T}_{x,W}[f_W](x). \tag{4}$$

The above definition postulates that the relevance of an input feature/node depends on the input mainly via the output function, although it can have a direct dependence on x and W.

In this paper, we demonstrate our novel BNN explanation framework mainly using Layer-wise Relevance Propagation (LRP) [28] as the base explanation method, however, we would like to stress that our BNN explanation framework can be applied for *any* existing explanation method.

a) Gradient explanation: The Gradient explanation method, i.e. $\mathcal{T}_{x,W} = \nabla_x$, where ∇_x is the weak derivative w.r.t. x, is one of the most basic explanation methods. It visualizes the possible extend of change made by the predictive function in a local neighbourhood around the original datapoint x [23], [27], [60].

b) LRP: Layer-wise Relevance Propagation [28] is a model-aware explanation technique that can be applied for feed-forward neural networks and can be used for different types of inputs, such as images, videos, or text [61], [62], [33], [43]. The underlying idea of the LRP algorithm is to use the network weights and the neural activations computed in the forward-pass to propagate the relevant output back through the network until the input layer is reached. This propagation procedure is subject to a conservation rule — analogous to Kirchoff's conservation laws in electrical circuits [63] — in each backpropagation step, the relevances from the output layer are distributed towards the input layer, while the sum of relevances should remain the same. Existing variations of LRP are, e.g., LRP-0, LRP-ε, LRP-γ, and LRP-CMP [28], [63].

c) Integrated gradients: Integrated Gradients [64] is an axiomatic local explanation algorithm that also addresses the "gradient saturation" issue [65]. It assigns relevance scores to each feature by approximating the integral of the gradients of the model output with respect to a scaled version of the input. The relevance attribution function, in this case, can be defined as

$$\mathcal{T}_{x,W}[f_W](x) = (x - \bar{x}) \odot \int_0^1 \frac{\partial f_W(\bar{x} + \alpha(x - \bar{x}))}{\partial x} d\alpha,$$

where $\odot$ denotes the element-wise product, and $\bar{x}$ is a *reference point* that represents the absence of a feature in the input.

III. XAI FOR BNNs

Despite the growing interest in Explainable AI, *Bayesian Neural Networks (BNN)* have so far lacked the attention of the
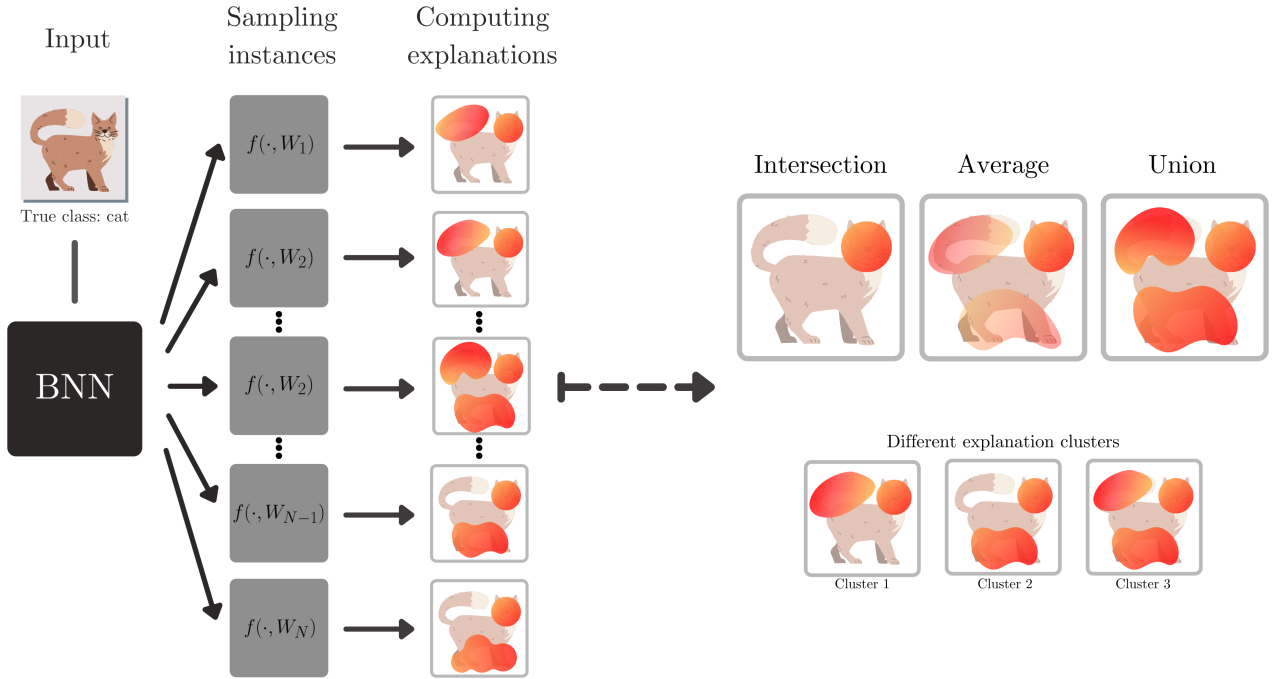
Fig. 2: Schematic illustration of proposed methods for explaining Bayesian Neural Networks. Given a particular input – a cat image – we sample models from the posterior distribution and collect local explanations. The Union explanation provides a global overview of the features learned by the BNN by combining various modes, whereas the intersection explanation provides the intersection strategy used by the BNN. Explanations can be further clustered to illustrate the main decision-making strategies.

XAI community. Most of the work on the topic of interpreting the BNNs concentrate on uncertainty quantification and visualization: [66] proposes a method to decompose the moment-based predictive uncertainty into two parts: aleatoric and epistemic: in [67] author proposes a model-agnostic method to visualize the contribution of individual features to predictive, epistemic and aleatoric uncertainty [66]. Recently, it has been shown that explanations of DNN can be enhanced by introducing stochasticities to the model weights [68], which, to some extend, lead to explanations similar to the ones using Diagonal or KFAC Laplace approximation. The so-called NoiseGrad method [68] adds multiplicative Gaussian noise to the model weights, which significantly reduces the gradient shattering effect [69] similar to the SmoothGrad method [70].

IV. EXPLAINING BAYESIAN NEURAL NETWORKS

In the following, we consider a neural network $f_W(x)$ and a relevance function $R_W(x)$ (defined in Eq. 10), using an arbitrary explanation method. Note that $R_W(x)$ is a deterministic mapping for a fixed parameter W. Therefore, the posterior distribution of parameter W induces a distribution over the relevances, resulting in a distribution over relevance maps. Given the posterior distribution of $W \sim p(W|\mathcal{D}_{\text{tr}})$, we can define the distribution of relevance as

$$p(R|\boldsymbol{x}, \mathcal{D}_{\text{tr}}) = \int R_W(x)p(W|\mathcal{D}_{\text{tr}})dW. \quad (5)$$

Relevance samples

$$R \sim p(R|\boldsymbol{x}, \mathcal{D}_{\text{tr}})$$

can be obtained by drawing weights from the posterior distribution:

$$W \sim p(W|\mathcal{D}_{\text{tr}}).$$

A schematic illustration of the process of obtaining the explanations, as well as a high-level overview of proposed methods could be found in Figure 2. Here, illustrative we can observe that different samples of the network lead to different explanations of the same input image. By applying aggregation strategies, such as the Intersection, Average, and Union strategy, the model behavior can be mapped more profoundly and could thus serve as support for a better comprehensibility for humans.

A. Average Explanation

For some conditions, the average relevance attribution coincides with the relevance attribution of the average prediction, which we state in the following Lemma:

Lemma 1: For any explanation method that can be formalized as in Eq.(10) with a linear operator $\mathcal{T}_{x,W} = \mathcal{T}_x$ that does not depend on W, it holds that

$$\mathcal{T}_x\left[\mathbb{E}_W\left[f_W\right]\right](x) = \mathbb{E}_W\left[\mathcal{T}_x[f_W](x)\right] = \mathbb{E}_W\left[R_W(x)\right]. \quad (6)$$

The claim holds trivially by the linearity assumption. Eq.(6) in the above Lemma holds for some existing explanation methods, including LRP-0, which is known to be expressed as Eq. (10) with $\mathcal{T}_{x,W}[f_W](x) = \mathcal{T}_x[f_W](x) = x \odot \nabla_x[f_W](x)$. One can still rely on Eq. (10) under a slight violation of linearity.
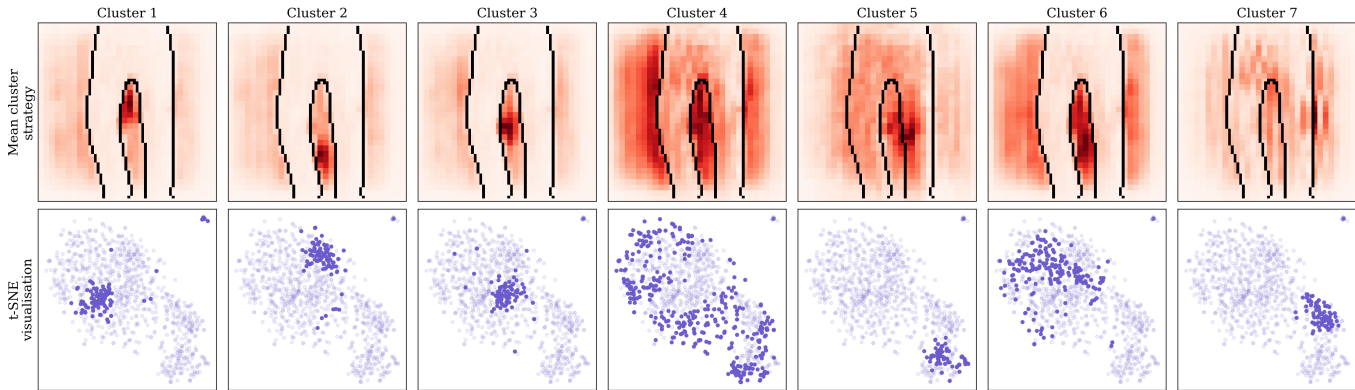
Fig. 3: Visualization of the multi-modality of Absolute gradient explanations of a BNN (here a LeNet network trained with dropout) are shown exemplary for an image of class "Trousers" from the Fashion MNIST dataset. The explanations were clustered by the SpRAy algorithm into 7 clusters, stated on top, and the first row shows the mean explanation for each cluster respectively, where the shape of the trouser is overlayed over the explanation. The second row depicts the t-SNE visualization of the distribution of explanations, where the points of the particular clusters are highlighted. From the mean cluster explanations, we can observe the variability in the decision-making process of the Bayesian Neural Networks — each mode illustrates one decision-making pattern and the number of elements in each cluster indicate the importance of each cluster to the prediction.

Theorem 1: Eq. (6) holds almost everywhere in $x \in \mathbb{R}^d$ for LRP-0 with ReLU networks, gradient explanation, and IG. The proof is given in the Appendix. Theorem 1 states that the explanation of the predictive mean (LHS of Eq.(6)) can be computed by the sample mean of the relevance maps over the posterior distribution (RHS of (6)).

This is beneficial since it is computationally exhausting to explain the approximate mean predictive function directly (this requires to simultaneously store all the parameters along with their computational graphs for each of the samples from the posterior distribution), using the results from Theorem 1 we can now easily explain it by sampling relevance maps, which drastically eases the process.

B. Exploring multi-modality of explanations

As a result of the non-linear network activations, BNNs are known to have multi-modal predictive functions [71]. Different parameters sampled from the posterior distribution can thus yield to noticeable differences in the decision-making process of the network as shown schematically in Figure 2. This, therefore, implies that when using the mean explanation, i.e., one of the simplest aggregation strategies to explain BNNs, we might lose intrinsic information about the variability of the decision-making processes of a BNN.

To investigate the "prime" strategies of the Bayesian learning machine and to decompose the behavior of BNNs into groups of inter-similar strategies, we propose to cluster the sampled explanations. Although our method does not restrict a user in choosing an algorithm for clustering, we propose to use the SpRAy (Spectral Relevance Analysis) clustering method. This method was initially introduced in [34] to solve a similar task — an analysis of the class-wise learned decision strategies of DNN in order to obtain a global view on the class related relevant patterns, which also supports the identification of undesirable behavior, such as clever Hans

artifacts (see Section VI-D for more information about clever Hans behavior). Note that SpRAy originally was constructed to investigate the typical traits in the decision-making process over a large collection of relevance maps, that were obtained from different data points from the training dataset. In contrast to the original setting of SpRAy, we now want to exhibit and understand typical as well as atypical behavior in the BNN decision-making process for a *single* input image.

Once the clustering has been performed, "prime" prediction strategies of the BNN for the given input image can be identified by the cluster-wise average explanations. Moreover, the number of saliency maps in each cluster (normalized by the number of sampled relevance maps) could be considered as the "strength" of each strategy. We could visualize the explanations, clusters, and average cluster strategies in a two-dimensional embedding using a t-SNE plot[72] as shown in Figure 3, where the explanations of the Fashion MNIST [73] input image is mainly divided into seven different clusters, which indicates the patterns of the main modes of the BNN. More practical details about the clustering process could be found in the appendix.

C. Union and Intersection Explanation

Grasping the multimodality of the network through explanations, can be done in several ways. Each relevance attribution map is an explanation for an individual instance of the Bayesian Neural Network. In our work, we observed that differences between instances of BNN are reflected in the multi-modal distribution of explanations. Therefore, to aggregate differences in explanations for Bayesian Neural Networks, we propose a method called **UAI**: Union and Intersection. The intuitive idea is illustrated in Figure 2. We treat the relevance of a BNN as a random variable that follows Eq.(5).
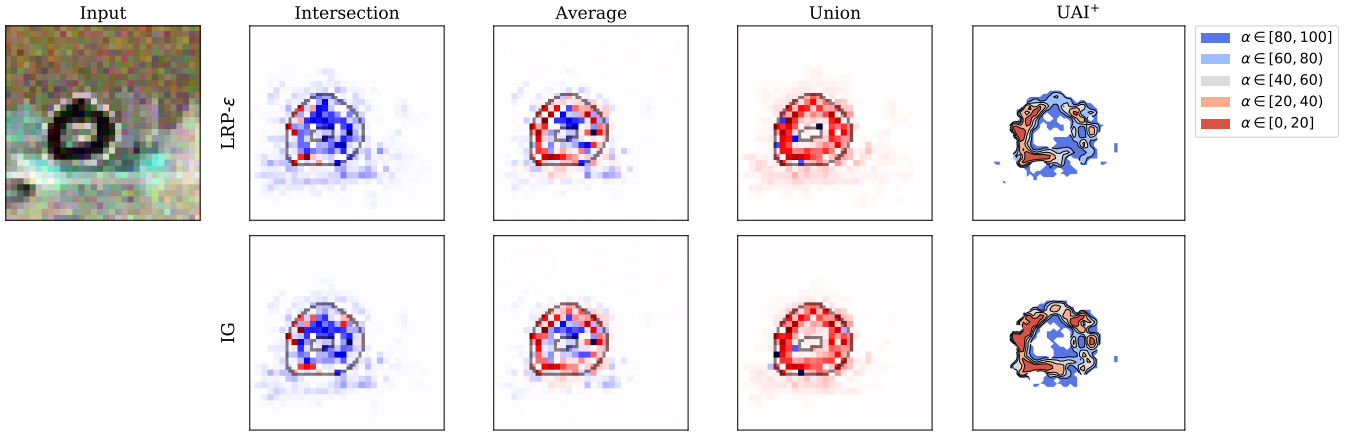
Fig. 4: Illustrative explanations of a Bayesian Neural Network. The BNN was trained with Dropout on the Custom MNIST dataset [68]. The input, an MNIST digit zero on a random CIFAR Background is shown on the left and was correctly classified as zero by the BNN. Explanations of the BNN decision are given as Intersection ($\alpha = 5$), Average, Union ($\alpha = 95$), and UAI$^+$ explanations using LRP-ε (first row), Integrated Gradient (IG) (second row). We can observe that the relevance of all explanations is emphasizing correctly the digit. However, our proposed Union and Intersection approach, in which the bundled information is contained in the UAI$^+$ explanation, has a stronger informational content about the role of the features concerning the model prediction by specifying the models (un)certainty that a feature contributed to the prediction made.

Given this distribution of relevance maps $p(R|\boldsymbol{x}, \mathcal{D}_{\text{tr}})$, we capture the uncertainty information of the BNN as follows:

$$\text{UAI}_\alpha(x) = \mathcal{P}_\alpha \left[p(R|\boldsymbol{x}, \mathcal{D}_{\text{tr}}) \right], \tag{7}$$

where $\mathcal{P}_\alpha$ is an operator computing the entry-wise (e.g. pixel-wise in case of images) percentiles.

High percentiles ($\alpha > 0.5$) correspond to what we introduce as Union explanation – a resulting relevance map consists of an accumulation of features of various relevance maps, i.e., providing information across modes of the BNN by allocating relevance to features that were considered of high importance by at least a small proportion of samples. In contrast to the Union explanation, small percentiles ($\alpha < 0.5$) illustrate the intersection of features, where at least 95% of the explanation agree on. For visualisations, we define Union explanations with $\alpha = 0.95$ and Intersection explanations with $\alpha = 0.05$

Furthermore, we introduce UAI$_\alpha^+$, as the uncertainty information of the BNN relating to positive class attributions only:

$$\text{UAI}^+(x) = \mathcal{F}_\epsilon \left[p(R|\boldsymbol{x}, \mathcal{D}_{\text{tr}}) \right], \tag{8}$$

where $\mathcal{F}_\epsilon$ is an operator computing the entry-wise (pixel-wise) probabilities of relevance attributed to particular pixel being less than some small predefined value $\epsilon > 0$. All proposed approaches (Intersection, Average, Union and UAI$^+$) are method-agnostic and the resulting LRP-ϵ and IG explanations are illustrated in Figure 4 for the case of MC Dropout network.

As scales of various explanation methods differ, in order to set ϵ that will threshold significant positive relevances we perform a *group normalization*: we normalize all positive relevances in all sampled attributions R_i by the maximum relevance value:

$$R_i^* = \frac{R_i}{\max \left(r_i^j | r_i^j \in R_i \; \forall i \in [1, N] \; \forall j \in [1, d] \right)}, \tag{9}$$

where N is the number of sampled attributions from the posterior and d is the number of features of the input. This way, we can set ϵ to a small value on the scale of $[0,1]$, such that it will threshold only significant positive relevances. In our visualisations, we set $\epsilon = 0.05$ as we empirically observe this value to be the borderline of visual recognition of positive relevances in the attribution map.

V. EVALUATION PROCEDURE

In the following, we provide the methodology of the qualitative and quantitative evaluation.

A. Qualitative Evaluation

For visual inspection of the results, we normalize the relevance maps with the MinMax transformation [28], that maps positive relevances onto the interval $[0, 1]$ and negative ones to $[-1, 0]$. Afterwards, the normalized relevance maps are visualized using the *'seismic'* colormap[2], which attributes red tones to pixels with positive relevances and blue tones to pixels with negative relevances.

B. Quantitative evaluation

For quantitative evaluation we use the localisation criterion: in the case of the localization criterion, we are interested in measuring the ability of an explanation method to attribute positive relevance to the object of interest. Hence, exemplary, if the prediction of a model is "cat", we assume that in the given image parts of the object cat are responsible for the prediction and subsequently yield positive relevance attribution by the explanation method. Thus, in order to correctly measure the ability of the method to "find" the object of interest,

---

[2]https://matplotlib.org/3.1.0/tutorials/colors/colormaps.html

ground-truth segmentations are required [74], [75], [76], [77], [78], [79], [68].

To measure the localization capability of an explanation method, we employ 2 different metrics, Area Under the ROC Curve and Relevance Mass Accuracy [74].

- **AUC ROC**: For each explanation (e.g., in form of a heatmap), we calculate the area under the receiver operating characteristic in order to measure how closely the areas of greatest relevance of the explanation correspond to the classified object. Note that for computing the AUC value, the pixel-wise ground-truth segmentation of the object serve as the true label information, whereas the relevance information from the explanation serve as the predicted label information.
- **Relevance Mass Accuracy (MA)**: For each explanation, we measure the proportion of the relevance mass that lies on the object in comparison to the total relevance mass:

$$MA = \frac{\sum_{i \in O} R_i}{\sum_{j \in I} R_j},$$

where I is the set containing all features and $O \subset I$ is a subset of features that are part of the segmented object itself.

While AUC metric can be used both for explanation methods attributing positive and negative values, as well as for methods attributing just positive relevances, for the correct usage of MA we filter only positive relevances from the explanation method.

C. Baseline

In our experiments, we compare the proposed UAI explanations with the baseline explanation, which uses the expected value of the weights $\mathbb{E}[W]$. In practice, this would corresponds to a MAP classifier, e.g., Laplace approximation or MC Dropout, where the mean weights of the model are used for prediction. Hence, we refer to the baseline explanation as the one explaining the standard deterministic model using the mean weights — this allows us to draw conclusions regarding how standard explanation methods can be enhanced by "Bayesianisation".

VI. EXPERIMENTS

In the following, we demonstrate the performance of our proposed method both qualitatively and quantitatively.

A. Experiment on Custom MNIST data

We evaluate our proposed methods on the Custom MNIST (CMNIST) dataset [68], where MNIST digits are plotted on a randomly chosen CIFAR background. This ensures that the decision-making basis for the model should rely only on the number and not on the randomly chosen background. Hence, using the available segmentations of the MNIST digits as a ground-truth indicator of the relevant area the evidence should be distributed to, we are able to measure the goodness of the different explanations. To show that our method is applicable to different types of Bayesian Neural Networks

and Network Ensembles we analyze three different settings all based on the same standard Lenet architecture [80]. We employ three different Bayesian approximation methods — Deep Ensemble of 100 different networks, trained with a random initialization respectively, Laplace approximation, and MC Dropout (more details about the model architecture and training parameters can be found in the appendix). Figure 5 illustrates the differences of UAI$^+$ explanations between the three Bayesian scenarios. For each of the three described scenarios, we used a test set of 10000 generated images, which was not used during training. For each image, $N = 100$ relevances were sampled using the LRP-ε method from the posterior distribution (in the case of a deep ensemble, each relevance came from a different network instance).

The quantitative results of the localization evaluation for all three scenarios are summarized in Table I. From the results, we can observe that the Union method is best-performing in terms of AUC metric, while the Intersection method shows overwhelmingly best results in terms of the Relevance Mass Accuracy metric. From these results we conclude that the Union method indeed is better in visualizing all the information the Bayesian Network has learned about the object, however, comparatively low MA scores of the Union method imply that explanations attribute positive relevance outside of the object of interest. In comparison, the Intersection method has low AUC scores in almost all scenarios, which imply that the Intersection method does not "cover" the object in interest with positive attributions, but high MA scores show high confidence in positive features — if the Intersection method attributes a positive relevance to a feature, it is most likely to lie inside of object of interest.

B. Experiment on Imagenet

We demonstrate the usefulness of the proposed method for explaining the decision-making process for a naturally non-Bayesian model that was trained with dropout regularization. We used the broadly applied pre-trained VGG16 network [81]. This network was pre-trained on Imagenet [82] and is naturally non-Bayesian. To access the uncertainty of this naturally non-Bayesian model, we employed MC Dropout [54] during the test phase, which can be always applied when a model's architecture comprises at least one dropout layer. Furthermore, as relevance attribution function, we used the LRP-CMP rule as explainability method. For the evaluation of the performance of the proposed methods, we randomly choose a small subset of classes from the Imagenet dataset, consisting of 5 classes: "castle", "lemon", "llama", "wine" and "tiger cat". For each class we downloaded[3] 1000 random images. The explanation results for the Intersection, Average, Union, and UAI$^+$ explanation for three randomly chosen images are shown in Figure 6.

C. Experiment on real-world cancer data

In the following, we perform a binary classification experiment, where the task is to classify histopathological images

---

[3]To download a subset of Imagenet dataset, the following library was used: https://github.com/mf1024/ImageNet-Datasets-Downloader.
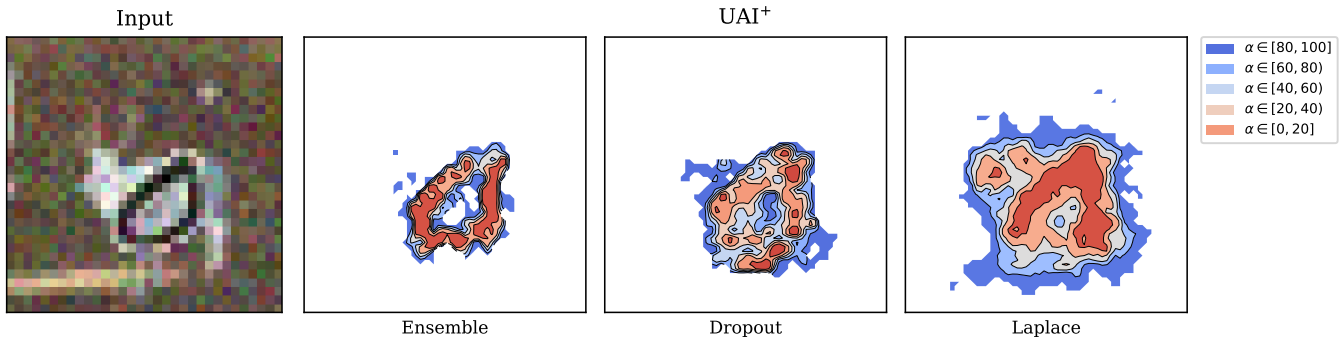
Fig. 5: Illustration of UAI$^+$ method explanations based on Absolute Gradient explanation method for 3 different Bayesian scenarios: Deep Ensemble, MC Dropout and Laplace approximation. From explanations we can observe main features that each of the Bayesian Network used.

TABLE I: Quantitative results for Localisation (AUC) and Relevance Mass Accuracy (MA). Each column represents the average score with standard deviation, only the Baseline explanation of the Deep Ensemble scenario is left blank as the MAP solution cannot be accessed in this scenario.

	Ensemble		Laplace Approximation		Dropout	
	AUC	MA	AUC	MA	AUC	MA
Random	0.4999 ± 0.0199	0.2497 ± 0.0093	0.5013 ± 0.0188	0.2506 ± 0.0094	0.4985 ± 0.0186	0.2497 ± 0.0095
Baseline	—	—	0.535 ± 0.0301	0.8464 ± 0.0966	0.5348 ± 0.0321	0.9179 ± 0.0665
Average	0.4971 ± 0.0541	0.9358 ± 0.0539	0.5034 ± 0.0573	$\textbf{0.8511} \pm \textbf{0.0927}$	0.5117 ± 0.0436	0.9143 ± 0.0671
Intersection ($\alpha = 5$)	0.1555 ± 0.0565	$\textbf{0.9999} \pm \textbf{0.0008}$	0.1486 ± 0.0715	0.7827 ± 0.4071	0.1702 ± 0.0611	$\textbf{0.9878} \pm \textbf{0.0324}$
Union ($\alpha = 95$)	$\textbf{0.8768} \pm \textbf{0.0517}$	0.7743 ± 0.0899	$\textbf{0.8631} \pm \textbf{0.0677}$	0.6998 ± 0.1291	$\textbf{0.8582} \pm \textbf{0.0507}$	0.8704 ± 0.0849
UAI$^+$	0.7855 ± 0.0581	0.8982 ± 0.0842	0.7831 ± 0.0647	0.7944 ± 0.1373	0.7142 ± 0.0497	0.9368 ± 0.0688

into cancer and non-cancer images. Clearly, the domain of diagnostic pathology requires not only accurate and robust predictions, but most importantly, explanations and insights about why an image was classified as cancerous or not by the learning machine (cf. also [41], [42], [43]).

The histopathological dataset consists of the 22302 patches of anonymized non-small-cell lung cancer (NSCLC) cases (n=200) from routine diagnostics from the archives of the Institute of Pathology at the Charité University Hospital which had been digitized using a 3DHistech P1000 whole slide scanner. The data had been annotated by board-certified pathologists for 28 different morphological classes ranging. For this experiment, we are interested only in the problem of binary classification for one class — carcinoma. The dataset is divided into 2 parts: training and testing. The training dataset consists of 17884 labeled patches, where 69.9% of the images are labeled as non-cancerous.

For this experiment, we trained a VGG-16 [81] network with an additional dropout regularization layer applied in the feature extractor part of the network (after the first and third MaxPool layer). The network was trained in a binary classification fashion for detecting the existence of cancer tissue in a histological slide. We trained the network for 100 epochs, using the cross-entropy loss with stochastic gradient descent, where the initial learning rate was set to 0.001. The trained network achieved an accuracy of 86.96% on the provided test dataset and an F1 score of 0.8205. Afterward, we computed the UAI explanations for different test images, which allows us to provide an additional estimate of the explanation uncertainty. Results for three different prototypical cancer images are

shown in Figure 7. The original histopathological image is shown in the left column with the black dots representing expert-labeled cancerous cells.

In the right column of Figure 7, the UAI results are plotted over the original image and highlight the relevant parts of the image regarding their importance for the classifier. In the Intersection explanation (second column from the left) we show the regions, in the image where the classifier is most certain about their relevance to the prediction "cancer", and with gray color, features that are absent from the Average explanation are highlighted. Analogous, for Union explanation we highlight features in green, that are attributed positively in the Union explanation, but not in the Average explanation. Thus we can visually observe differences between Intersection, Average, and Union explanations — while Intersection explanations provide a user with more "conservative" explanations, the Union method allows to observe all the features, that were considered with positive evidence towards the class in question. From the quantitative results shown in Table II we can observe that the higher the percentile value the larger the AUC score for the localization criteria of the cancerous cells. Note that in the quantitative experiment we used only the images labeled as cancerous, where the annotations of the cancerous areas were available.

In general, the UAI-based heatmaps with different α values can prove particularly useful with respect to different diagnostic applications. Low α value explanations can help to identify tissue regions with the highest likelihood of cancer. High α percentile explanations may then be used for AI-based screening applications, where it is important not to overlook
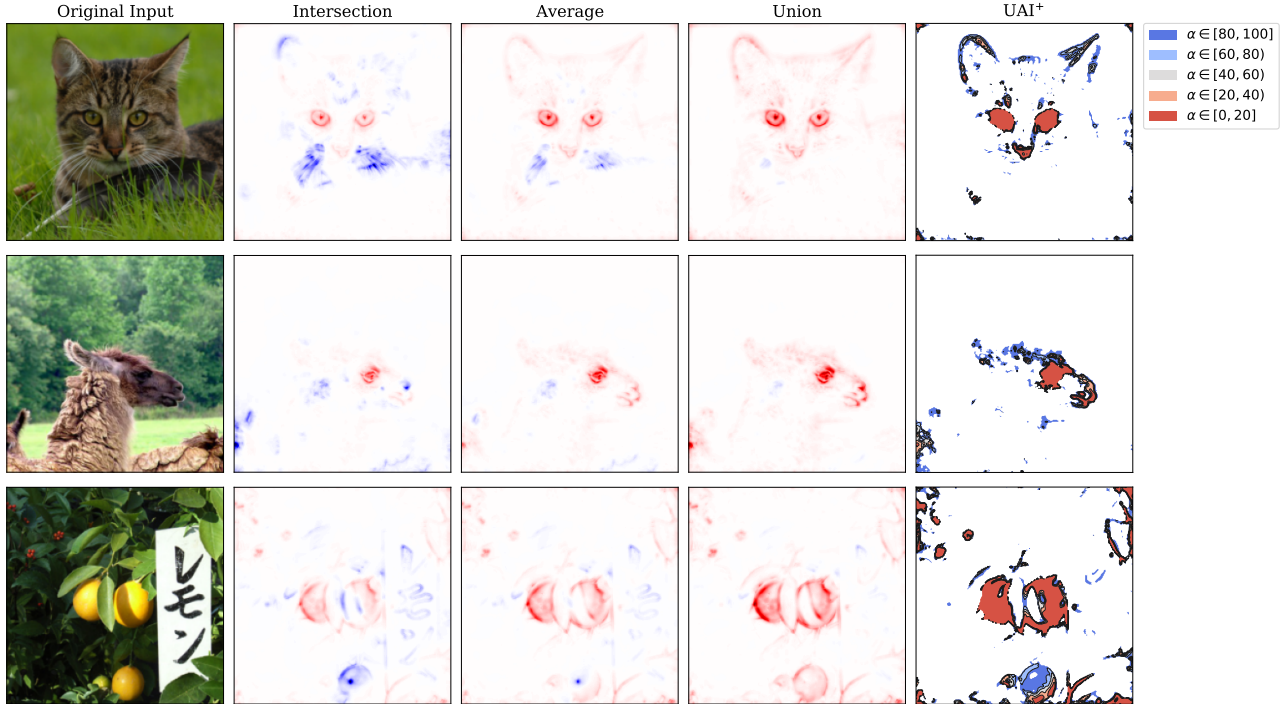
Fig. 6: Exemplary explanations of three images taken from Imagenet (red/blue indicates positive/negative relevance). Each row corresponds to a particular input image. From left to right: original image, intersection explanation, baseline (average LRP) explanation, and Union explanations, as well as the UAI$^+$ explanation. We observe that the baseline explanation attributes positive relevance to almost the whole cat except the whiskers. The intersection explanation highlights solely the eyes and the nose of the cat as coherent features whereas the union explanation highlights the same features as the baseline explanation but additionally attributes relevance to the whiskers. The explanation of UAI$^+$ provides a holistic representation of the different feature importance regarding the model decision: red=high importance, (orange, grey, light blue)=intermediate importance, and dark blue=low importance.

TABLE II: Localisation results of different Bayesian explanations methods for detecting malignent cancer cells. We observe that the Union explanation with $\alpha = 99$ achieves the best performance in this experiment.

Method		AUC Score
Baseline		0.6534 ± 0.1705
Average		0.6635 ± 0.1712
UAI	$\alpha = 1$	0.5960 ± 0.1733
	$\alpha = 5$	0.6138 ± 0.1742
	$\alpha = 25$	0.6536 ± 0.1716
	$\alpha = 50$	0.6818 ± 0.1711
	$\alpha = 75$	0.7026 ± 0.1717
	$\alpha = 95$	0.7179 ± 0.1694
	$\alpha = 99$	$\mathbf{0.7201 \pm 0.1680}$

even the tiniest occurrence of tumor cells in tissue samples. Therefore, combining UAI analyses with low and high α may provide high sensitivity and simultaneously points the pathologists to regions where the machine is most confident about its decision. This additional information will improve diagnostic speed and also reduce the risk of overlooking crucial information in the diagnostic process.

D. Confirming Clever Hans Effect

In the following experiment, we revisit the work of Lapuschkin et al. [76], [34], [35] on the *clever Hans* effect. A *clever Hans* strategy denotes a problematic solution strategy that provides the right answer for the wrong reason: the classic example being the one of the horse Hans, which was able to correctly provide answers to simple computation questions while actually not doing math but rather reading its master. A modern machine-learning example is an artifact or a watermark in the data that happens to be present in one class, i.e., there is a random artifactual correlation that the model systematically and erroneously harvests [76], [34]. The following experiment was conducted on the Pascal Voc 2007 dataset, where, as shown in [34] a clever Hans behavior is learned for the class horse (the detailed experiment description can be found in the appendix). The UAI explanations with respect to the class *horse* are illustrated in Figures 8. We indeed observe the fact that the watermark in the bottom left corner of the image occurs with a high relevance on both images in the 5-th percentile explanation. In other words, 95% of the samples of relevance maps consider this feature to highly contribute to the class "horse". Given this finding, we can confirm that the *clever Hans* is really clever, in the sense that the classification is based on the information from
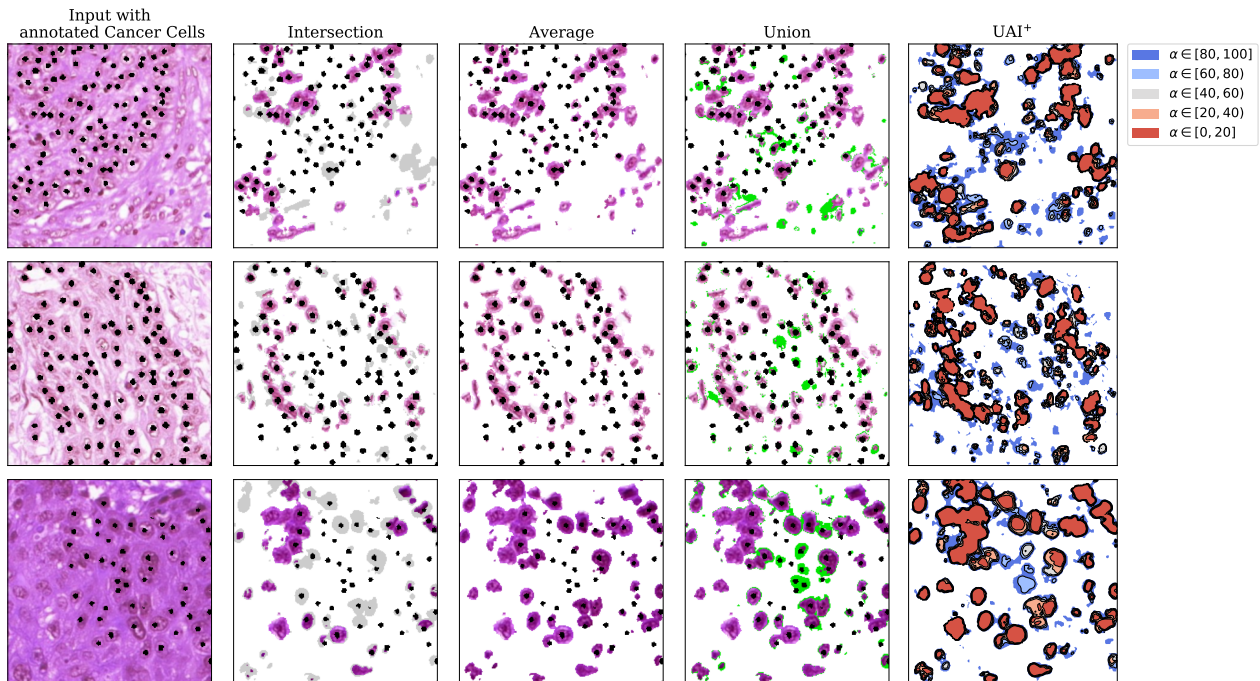
Fig. 7: Comparison of the explanation results for the cancer experiment. A VGG16 [81] was trained on a set of Haematoxylin-eosin-stained Lung adeno carcinoma (LUAD) as well as on non cancer histological slides. Three original images labeled as cancer, taken from the test set, are shown on the left, overlaid with black dots, which represent the cancer cells annotated by experts. Behind, the various explanations of the model prediction for the class cancer are shown from left to right as intersection, baseline, union, and UAI$^+$ explanation. For reporting only significant positive relevances, we set a threshold at $\varepsilon = 0.05$ and visualize only relevances that surpass this threshold. We highlight by grey and green the additional information gained by our union and intersection approach in comparison to the baseline explanation. In detail, the intersection is highlighting the most certain areas, which are indicated as parts of the original image, whereas the areas that are not certain, and thus not visualized in the intersection explanation are highlighted in grey. In contrast, the union explanation identifies additional information, which was not shown in the baseline explanation and therefore may point out new areas that may be cancerous, which are highlighted in green. The aggregation of the diverse level of feature importance is summarized in the UAI$_+$ explanation shown on the right.
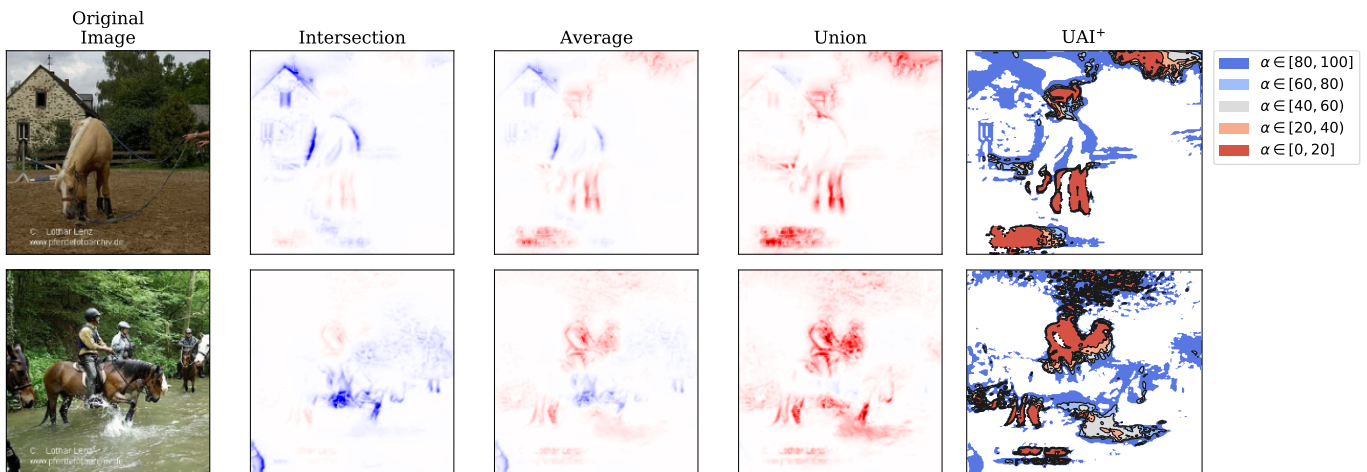

Fig. 8: Exemplary visualization of the *clever hans* effect for two images, taken from the Pascal Voc 2007 dataset, depicting a horse respectively. UAI explanations help the user to distinguish between random artifacts on the explanations and systematic behaviour of the learning machine. UAI$^+$ allows us to confirm that the clever Hans effect exists with high certainty (red) on the watermark (top) and on the human riding the horse (bottom).

the learned artifact. Thus, the proposed UAI method enable us to distinguish between systematic behavior and potential explainability artifacts (see e.g. [83], [84], [19]).

VII. CONCLUDING DISCUSSION

When tackling real-world learning problems, Bayesian models have been helpful to assess the intrinsic uncertainties encountered when predicting. The field of XAI could introduce a further safety layer into the inference process when using neural networks because explanations can contribute to, e.g., unmasking flaws in a model or data set [34]. So far, however, no XAI method for Bayesian Neural Networks was conceived.

In this paper, we have therefore connected the BNN model class (and their inbuilt uncertainty quantification) with XAI by proposing the (to the best of our knowledge) first practical method for explaining BNNs. As demonstrated, our novel technique (called UAI) is applicable to several popular explanation methods.

By appropriately averaging sampled relevance maps, we can obtain an explanation for the expected predictive function. This allows us to shed light on the decision-making process of BNNs: interestingly, UAI allows us to not only inspect the most relevant pixels for a decision but also their (un)certainties. Our method is thus a formidable starting point for obtaining novel insight into the behavior of Bayesian learning models.

We found that, with a high parameter range of α, UAI explains the behavior of the network more informatively, in comparison to a standard mean explanation baseline. By gauging α, users can understand the rationale behind a network: with small parameters of α, we can observe what features are considered to be contributing towards the prediction regardless of the sampled strategy (intersection explanation). With high parameters α, we can understand the features for which at least a small fraction of strategies attribute them with positive relevance (union explanation). Thus, by choosing the parameter α, users can choose between more or less risk-averse explanations, depending on the task objective. The proposed UAI explanation additionally helps to understand and reflect the multiple explanation modes inherent in a Bayesian ensemble (cf. Figure 2).

The computational complexity of UAI is linear in the number of posterior samples. Already as few as 100 samples turned out to be sufficient for a stable assessment of the explanation uncertainty on a coarse grain in our experiments.

Concluding, our UAI framework now enables a wide range of explanation methods to analyze the complex multi-faceted decision-making process of Bayesian Neural Networks. Moreover, this novel possibility of quantifying uncertainties in explanations of trained Neural Networks may become a profound help to mitigate risks in safety-critical applications. Future studies will focus further on clinical decision-making systems.

ACKNOWLEDGEMENTS

REFERENCES

[1] Q. Xie, M.-T. Luong, E. Hovy, and Q. V. Le, "Self-training with noisy student improves imagenet classification," in *Proceedings of the IEEE/CVF Conference on Computer Vision and Pattern Recognition*, 2020, pp. 10 687–10 698.

[2] H. Touvron, A. Vedaldi, M. Douze, and H. Jégou, "Fixing the train-test resolution discrepancy: Fixefficientnet," *arXiv preprint arXiv:2003.08237*, 2020.

[3] C. Szegedy, V. Vanhoucke, S. Ioffe, J. Shlens, and Z. Wojna, "Rethinking the inception architecture for computer vision," in *Proceedings of the IEEE conference on computer vision and pattern recognition*, 2016, pp. 2818–2826.

[4] S. Edunov, M. Ott, M. Auli, and D. Grangier, "Understanding back-translation at scale," *arXiv preprint arXiv:1808.09381*, 2018.

[5] M. Shoeybi, M. Patwary, R. Puri, P. LeGresley, J. Casper, and B. Catanzaro, "Megatron-lm: Training multi-billion parameter language models using gpu model parallelism," *arXiv preprint arXiv:1909.08053*, 2019.

[6] C. Raffel, N. Shazeer, A. Roberts, K. Lee, S. Narang, M. Matena, Y. Zhou, W. Li, and P. J. Liu, "Exploring the limits of transfer learning with a unified text-to-text transformer," *arXiv preprint arXiv:1910.10683*, 2019.

[7] Z. Yang, Z. Dai, Y. Yang, J. Carbonell, R. R. Salakhutdinov, and Q. V. Le, "Xlnet: Generalized autoregressive pretraining for language understanding," in *Advances in neural information processing systems*, 2019, pp. 5753–5763.

[8] A. Ecoffet, J. Huizinga, J. Lehman, K. O. Stanley, and J. Clune, "Go-explore: a new approach for hard-exploration problems," *arXiv preprint arXiv:1901.10995*, 2019.

[9] D. Silver, T. Hubert, J. Schrittwieser, I. Antonoglou, M. Lai, A. Guez, M. Lanctot, L. Sifre, D. Kumaran, T. Graepel *et al.*, "Mastering chess and shogi by self-play with a general reinforcement learning algorithm," *arXiv preprint arXiv:1712.01815*, 2017.

[10] D.-O. Won, K.-R. Müller, and S.-W. Lee, "An adaptive deep reinforcement learning framework enables curling robots with human-like performance in real-world conditions," *Science Robotics*, vol. 5, no. 46, 2020.

[11] B. Goertzel and C. Pennachin, *Artificial general intelligence*. Springer, 2007, vol. 2.

[12] K. He, X. Zhang, S. Ren, and J. Sun, "Delving deep into rectifiers: Surpassing human-level performance on imagenet classification," in *Proceedings of the IEEE international conference on computer vision*, 2015, pp. 1026–1034.

[13] O. Vinyals, T. Ewalds, S. Bartunov, P. Georgiev, A. S. Vezhnevets, M. Yeo, A. Makhzani, H. Küttler, J. Agapiou, J. Schrittwieser *et al.*, "Starcraft ii: A new challenge for reinforcement learning," *arXiv preprint arXiv:1708.04782*, 2017.

[14] X. Liu, P. He, W. Chen, and J. Gao, "Improving multi-task deep neural networks via knowledge distillation for natural language understanding," *arXiv preprint arXiv:1904.09482*, 2019.

[15] T. B. Brown, B. Mann, N. Ryder, M. Subbiah, J. Kaplan, P. Dhariwal, A. Neelakantan, P. Shyam, G. Sastry, A. Askell *et al.*, "Language models are few-shot learners," *arXiv preprint arXiv:2005.14165*, 2020.

[16] M. M.-C. Vidovic, N. Görnitz, K.-R. Müller, G. Rätsch, and M. Kloft, "Opening the black box: Revealing interpretable sequence motifs in kernel-based learning algorithms," in *Joint European Conference on Machine Learning and Knowledge Discovery in Databases*. Springer, 2015, pp. 137–153.

[17] V. Buhrmester, D. Münch, and M. Arens, "Analysis of explainers of black box deep neural networks for computer vision: A survey," *arXiv preprint arXiv:1911.12116*, 2019.

[18] V. H. Buch, I. Ahmed, and M. Maruthappu, "Artificial intelligence in medicine: current trends and future possibilities," *British Journal of General Practice*, vol. 68, no. 668, pp. 143–144, 2018.

[19] W. Samek, G. Montavon, A. Vedaldi, L. K. Hansen, and K.-R. Müller, Eds., *Explainable AI: Interpreting, Explaining and Visualizing Deep Learning*, ser. Lecture Notes in Computer Science. Springer, 2019, vol. 11700.

[20] A. Adadi and M. Berrada, "Peeking inside the black-box: a survey on explainable artificial intelligence (xai)," *IEEE access*, vol. 6, pp. 52 138–52 160, 2018.

[21] A. Das and P. Rad, "Opportunities and challenges in explainable artificial intelligence (xai): A survey," *arXiv preprint arXiv:2006.11371*, 2020.

[22] E. Tjoa and C. Guan, "A survey on explainable artificial intelligence (xai): Toward medical xai," *IEEE Transactions on Neural Networks and Learning Systems*, 2020.

[23] D. Erhan, Y. Bengio, A. Courville, and P. Vincent, "Visualizing higher-layer features of a deep network," *University of Montreal*, vol. 1341, no. 3, p. 1, 2009.

[24] A. Nguyen, A. Dosovitskiy, J. Yosinski, T. Brox, and J. Clune, "Synthesizing the preferred inputs for neurons in neural networks via deep generator networks," in *Advances in neural information processing systems*, 2016, pp. 3387–3395.

[25] A. Nguyen, J. Yosinski, and J. Clune, "Multifaceted feature visualization: Uncovering the different types of features learned by each neuron in deep neural networks," *arXiv preprint arXiv:1602.03616*, 2016.

[26] M. M.-C. Vidovic, M. Kloft, K.-R. Mueller, and N. Goernitz, "Ml2motif—reliable extraction of discriminative sequence motifs from learning machines," *PloS one*, vol. 12, no. 3, p. e0174392, 2017.

[27] D. Baehrens, T. Schroeter, S. Harmeling, M. Kawanabe, K. Hansen, and K.-R. Müller, "How to explain individual classification decisions," *Journal of Machine Learning Research*, vol. 11, no. Jun, pp. 1803–1831, 2010.

[28] S. Bach, A. Binder, G. on, F. Klauschen, K.-R. Müller, and W. Samek, "On pixel-wise explanations for non-linear classifier decisions by layer-wise relevance propagation," *PloS one*, vol. 10, no. 7, 2015.

[29] M. M.-C. Vidovic, N. Görnitz, K.-R. Müller, and M. Kloft, "Feature importance measure for non-linear learning algorithms," *arXiv preprint arXiv:1611.07567*, 2016.

[30] R. R. Selvaraju, M. Cogswell, A. Das, R. Vedantam, D. Parikh, and D. Batra, "Grad-cam: Visual explanations from deep networks via gradient-based localization," in *Proceedings of the IEEE international conference on computer vision*, 2017, pp. 618–626.

[31] J. Yosinski, J. Clune, A. Nguyen, T. Fuchs, and H. Lipson, "Understanding neural networks through deep visualization," *arXiv preprint arXiv:1506.06579*, 2015.

[32] P.-J. Kindermans, K. T. Schütt, M. Alber, K.-R. Müller, D. Erhan, B. Kim, and S. Dähne, "Learning how to explain neural networks: Patternnet and patternattribution," *arXiv preprint arXiv:1705.05598*, 2017.

[33] G. Montavon, W. Samek, and K.-R. Müller, "Methods for interpreting and understanding deep neural networks," *Digital Signal Processing*, vol. 73, pp. 1–15, 2018.

[34] S. Lapuschkin, S. Wäldchen, A. Binder, G. on, W. Samek, and K.-R. Müller, "Unmasking clever hans predictors and assessing what machines really learn," *Nature communications*, vol. 10, p. 1096, 2019.

[35] W. Samek, G. Montavon, S. Lapuschkin, C. J. Anders, and K.-R. Müller, "Explaining deep neural networks and beyond: A review of methods and applications," *Proceedings of the IEEE*, vol. 109, no. 3, pp. 247–278, 2021.

[36] S. M. Lundberg and S.-I. Lee, "A unified approach to interpreting model predictions," in *Advances in neural information processing systems*, 2017, pp. 4765–4774.

[37] S. M. Lundberg, G. Erion, H. Chen, A. DeGrave, J. M. Prutkin, B. Nair, R. Katz, J. Himmelfarb, N. Bansal, and S.-I. Lee, "From local explanations to global understanding with explainable ai for trees," *Nature Machine Intelligence*, vol. 2, no. 1, pp. 2522–5839, 2020.

[38] A.-K. Dombrowski, C. J. Anders, K.-R. Müller, and P. Kessel, "Towards robust explanations for deep neural networks," *Pattern Recognition*, p. 108194, 2021.

[39] A. Janowczyk and A. Madabhushi, "Deep learning for digital pathology image analysis: A comprehensive tutorial with selected use cases," *Journal of pathology informatics*, vol. 7, 2016.

[40] A. Cruz-Roa, A. Basavanhally, F. González, H. Gilmore, M. Feldman, S. Ganesan, N. Shih, J. Tomaszewski, and A. Madabhushi, "Automatic detection of invasive ductal carcinoma in whole slide images with convolutional neural networks," in *Medical Imaging 2014: Digital Pathology*,

[41] vol. 9041. International Society for Optics and Photonics, 2014, p. 904103.

[41] F. Klauschen, K.-R. Müller, A. Binder, M. Bockmayr, M. Hägele, P. Seegerer, S. Wienert, G. Pruneri, S. de Maria, S. Badve *et al.*, "Scoring of tumor-infiltrating lymphocytes: From visual estimation to machine learning," in *Seminars in cancer biology*, vol. 52. Elsevier, 2018, pp. 151–157.

[42] M. Hägele, P. Seegerer, S. Lapuschkin, M. Bockmayr, W. Samek, F. Klauschen, K.-R. Müller, and A. Binder, "Resolving challenges in deep learning-based analyses of histopathological images using explanation methods," *Scientific reports*, vol. 10, p. 6423, 2020.

[43] A. Binder, M. Bockmayr, M. Hägele, S. Wienert, D. Heim, K. Hellweg, M. Ishii, A. Stenzinger, A. Hocke, C. Denkert *et al.*, "Morphological and molecular breast cancer profiling through explainable machine learning," *Nature Machine Intelligence*, vol. 3, no. 4, pp. 355–366, 2021.

[44] D. Hendrycks and K. Gimpel, "A baseline for detecting misclassified and out-of-distribution examples in neural networks," *arXiv preprint arXiv:1610.02136*, 2016.

[45] N. Srivastava, G. Hinton, A. Krizhevsky, I. Sutskever, and R. Salakhutdinov, "Dropout: a simple way to prevent neural networks from overfitting," *The journal of machine learning research*, vol. 15, no. 1, pp. 1929–1958, 2014.

[46] P. De Laplace, "Mémoire sur les suites récurro-récurrentes et sur leurs usages dans la théorie des hasards," *Mém. Acad. Roy. Sci. Paris*, vol. 6, pp. 353–371, 1774.

[47] H. Ritter, A. Botev, and D. Barber, "A scalable laplace approximation for neural networks," in *6th International Conference on Learning Representations, ICLR 2018-Conference Track Proceedings*, vol. 6. International Conference on Representation Learning, 2018.

[48] A. G. Wilson, "The case for bayesian deep learning," *arXiv preprint arXiv:2001.10995*, 2020.

[49] A. Holzinger, G. Langs, H. Denk, K. Zatloukal, and H. Müller, "Causability and explainability of artificial intelligence in medicine," *Wiley Interdisciplinary Reviews: Data Mining and Knowledge Discovery*, vol. 9, no. 4, p. e1312, 2019.

[50] J. Koo, J. Kwac, W. Ju, M. Steinert, L. Leifer, and C. Nass, "Why did my car just do that? explaining semi-autonomous driving actions to improve driver understanding, trust, and performance," *International Journal on Interactive Design and Manufacturing (IJIDeM)*, vol. 9, no. 4, pp. 269–275, 2015.

[51] G. Wiegand, M. Schmidmaier, T. Weber, Y. Liu, and H. Hussmann, "I drive-you trust: Explaining driving behavior of autonomous cars," in *Extended Abstracts of the 2019 CHI Conference on Human Factors in Computing Systems*, 2019, pp. 1–6.

[52] A. Graves, "Practical variational inference for neural networks," in *Advances in NIPS*, 2011.

[53] K. Osawa, S. Swaroop, A. Jain, R. Eschenhagen, R. E. Turner, R. Yokota, and M. E. Khan, "Practical deep learning with Bayesian principles," in *Advances in NeurIPS*, 2019.

[54] Y. Gal and Z. Ghahramani, "Dropout as a Bayesian approximation: Representing model uncertainty in deep learning," in *Proceedings of ICML*, 2016.

[55] D. P. Kingma, T. Salimans, and M. Welling, "Variational dropout and the local reparameterization trick," in *Advances in NIPS*, 2015.

[56] D. Molchanov, A. Ashukha, and D. Vetrov, "Variational dropout sparsifies deep neural networks," in *Proceedings of ICML*, 2017.

[57] F. Wenzel, K. Roth, B. S. Veeling, J. Swiatkowski, L. Tran, S. Mandt, J. Snoek, T. Salimans, R. Jenatton, and S. Nowozin, "How good is the bayes posterior in deep neural networks really?" *arXiv:2002.02405*, 2020.

[58] W. J. Maddox, P. Izmailov, T. Garipov, D. P. Vetrov, and A. G. Wilson, "A simple baseline for bayesian uncertainty in deep learning," in *Advances in NeurIPS*, 2019.

[59] A. G. Wilson and P. Izmailov, "Bayesian deep learning and a probabilistic perspective of generalization," in *Advances in NeurIPS*, 2020.

[60] K. Simonyan, A. Vedaldi, and A. Zisserman, "Deep inside convolutional networks: Visualising image classification models and saliency maps," *arXiv preprint arXiv:1312.6034*, 2013.

[61] C. J. Anders, G. Montavon, W. Samek, and K.-R. Müller, "Understanding patch-based learning of video data by explaining predictions," in *Explainable AI: Interpreting, Explaining and Visualizing Deep Learning*. Springer, 2019, pp. 297–309.

[62] L. Arras, F. Horn, G. Montavon, K.-R. Müller, and W. Samek, "" what is relevant in a text document?": An interpretable machine learning approach," *PloS one*, vol. 12, no. 8, p. e0181142, 2017.

[63] G. Montavon, A. Binder, S. Lapuschkin, W. Samek, and K.-R. Müller, "Layer-wise relevance propagation: an overview," in *Explainable AI: Interpreting, Explaining and Visualizing Deep Learning*. Springer, 2019, pp. 193–209.

[64] M. Sundararajan, A. Taly, and Q. Yan, "Axiomatic attribution for deep networks," *arXiv preprint arXiv:1703.01365*, 2017.

[65] W. Samek, A. Binder, G. on, S. Lapuschkin, and K.-R. Müller, "Evaluating the visualization of what a deep neural network has learned," *IEEE transactions on neural networks and learning systems*, vol. 28, no. 11, pp. 2660–2673, 2016.

[66] Y. Kwon, J.-H. Won, B. J. Kim, and M. C. Paik, "Uncertainty quantification using bayesian neural networks in classification: Application to biomedical image segmentation," *Computational Statistics & Data Analysis*, vol. 142, p. 106816, 2020.

[67] L. R. Chai, "Uncertainty estimation in bayesian neural networks and links to interpretability," *Master of Philosophy (University of Cambridge)*, 2018.

[68] K. Bykov, A. Hedström, S. Nakajima, and M. M.-C. Höhne, "Noisegrad: enhancing explanations by introducing stochasticity to model weights," *arXiv preprint arXiv:2106.10185*, 2021.

[69] W. Samek, G. Montavon, S. Lapuschkin, C. J. Anders, and K.-R. Müller, "Explaining deep neural networks and beyond: A review of methods and applications," *Proceedings of the IEEE*, vol. 109, no. 3, pp. 247–278, 2021.

[70] D. Smilkov, N. Thorat, B. Kim, F. Viégas, and M. Wattenberg, "Smoothgrad: removing noise by adding noise," *arXiv preprint arXiv:1706.03825*, 2017.

[71] C. M. Bishop, *Pattern recognition and machine learning*. springer, 2006.

[72] L. v. d. Maaten and G. Hinton, "Visualizing data using t-sne," *Journal of machine learning research*, vol. 9, no. Nov, pp. 2579–2605, 2008.

[73] H. Xiao, K. Rasul, and R. Vollgraf, "Fashion-mnist: a novel image dataset for benchmarking machine learning algorithms," *arXiv preprint arXiv:1708.07747*, 2017.

[74] L. Arras, A. Osman, and W. Samek, "Ground truth evaluation of neural network explanations with clevr-xai," *arXiv preprint arXiv:2003.07258*, 2020.

[75] J. Theiner, E. Müller-Budack, and R. Ewerth, "Interpretable semantic photo geolocalization," 2021.

[76] S. Lapuschkin, A. Binder, G. Montavon, K.-R. Müller, and W. Samek, "Analyzing classifiers: Fisher vectors and deep neural networks," in *Proceedings of the IEEE Conference on Computer Vision and Pattern Recognition*, 2016, pp. 2912–2920.

[77] M. Kohlbrenner, A. Bauer, S. Nakajima, A. Binder, W. Samek, and S. Lapuschkin, "Towards best practice in explaining neural network decisions with lrp," 2020.

[78] J. Zhang, Z. Lin, J. Brandt, X. Shen, and S. Sclaroff, "Top-down neural attention by excitation backprop," 2016.

[79] T. Fawcett, "An introduction to roc analysis," *Pattern Recogn. Lett.*, vol. 27, no. 8, p. 861–874, Jun. 2006. [Online]. Available: https://doi.org/10.1016/j.patrec.2005.10.010

[80] Y. LeCun, L. Bottou, Y. Bengio, and P. Haffner, "Gradient-based learning applied to document recognition," *Proceedings of the IEEE*, vol. 86, no. 11, pp. 2278–2324, 1998.

[81] K. Simonyan and A. Zisserman, "Very deep convolutional networks for large-scale image recognition," *arXiv preprint arXiv:1409.1556*, 2014.

[82] O. Russakovsky, J. Deng, H. Su, J. Krause, S. Satheesh, S. Ma, Z. Huang, A. Karpathy, A. Khosla, M. Bernstein *et al.*, "Imagenet large scale visual recognition challenge," *International journal of computer vision*, vol. 115, no. 3, pp. 211–252, 2015.

[83] A.-K. Dombrowski, M. Alber, C. Anders, M. Ackermann, K.-R. Müller, and P. Kessel, "Explanations can be manipulated and geometry is to blame," in *Advances in Neural Information Processing Systems*, 2019, pp. 13 567–13 578.

[84] J. Heo, S. Joo, and T. Moon, "Fooling neural network interpretations via adversarial model manipulation," *Advances in Neural Information Processing Systems*, vol. 32, pp. 2925–2936, 2019.

[85] U. Von Luxburg, "A tutorial on spectral clustering," *Statistics and computing*, vol. 17, no. 4, pp. 395–416, 2007.

[86] B. Léon, "Online algorithms and stochastic approximations," *Online Learning and Neural Networks; Cambridge University Press: Cambridge, UK*, 1998.

[87] M. Humt, J. Lee, and R. Triebel, "Bayesian optimization meets laplace approximation for robotic introspection," *arXiv preprint arXiv:2010.16141*, 2020.

[88] J. Lee, M. Humt, J. Feng, and R. Triebel, "Estimating model uncertainty of neural networks in sparse information form," in *International Conference on Machine Learning (ICML)*. Proceedings of Machine Learning Research, 2020.

Kirill Bykov received his Master's double degree in Computer Science at Technical University of Berlin as part of EIT Digital Data Science double degree program with Eindhoven University of Technology. Previously, Kirill earned his Bachelor's degree in Applied Mathematics from Saint-Petersburg State University. KB is interested in Deep Learning, Bayesian Learning and Explainable AI. Currently, he is pursuing his PhD at the Department of Machine Learning at TU Berlin and is a part of the UMI Lab research group. Since 2021 he is a fellow of the BIFOLD graduate school.

Marina M.-C. Höhne (née Vidovic) received her masters degree in Technomathematics from the Technical University of Berlin in 2012. Afterwards she worked as a researcher at Ottobock in Vienna, Austria, on time series data and domain adaptation for controlling prosthetic devices. In 2014 she started her PhD on explainable AI and received the Dr. rer. nat. degree from the Technical University of Berlin in 2017. After one year maternal leave, she continued working at the machine learning chair at TU Berlin as a postdoctoral researcher. In 2020 she started her own research group UMI Lab dealing with explainable artificial intelligence at the Technical University of Berlin. Moreover, since 2021 she is a junior fellow at the Berlin Institute for Foundations of Learning and Data and a fellow of the ProFiL excellence program. Since 2021 she has a secondary employment as Associate Professor at the Arctic University of Norway.

Adelaida Creosteanu Adelaida Creosteanu is a Machine Learning Engineer at Aignostics. In 2019, she earned a BSc Computer Science from the University of Southampton, UK, focusing on ML in her final year with a dissertation on skin cancer detection. She is interested in Deep Learning and Software Engineering in medical applications.

Klaus-Robert Müller (Member, IEEE) has been a professor of computer science at Technische Universität Berlin since 2006; at the same time he is directing and co-directing the Berlin Machine Learning Center and the Berlin Big Data Center, respectively. He studied physics in Karlsruhe from 1984 to 1989 and obtained his Ph.D. degree in computer science at Technische Universität Karlsruhe in 1992. After completing a postdoctoral position at GMD FIRST in Berlin, he was a research fellow at the University of Tokyo from 1994 to 1995. In 1995, he founded the Intelligent Data Analysis group at GMD-FIRST (later Fraunhofer FIRST) and directed it until 2008. From 1999 to 2006, he was a professor at the University of Potsdam. He was awarded the Olympus Prize for Pattern Recognition (1999), the SEL Alcatel Communication Award (2006), the Science Prize of Berlin by the Governing Mayor of Berlin (2014), the Vodafone Innovations Award (2017). In 2012, he was elected member of the German National Academy of Sciences-Leopoldina, in 2017 of the Berlin Brandenburg Academy of Sciences and also in 2017 external scientific member of the Max Planck Society. In 2019 and 2020 he became a Highly Cited researcher in the cross-disciplinary area. His research interests are intelligent data analysis and Machine Learning in the sciences (Neuroscience (specifically Brain-Computer Interfaces), Physics, Chemistry) and in industry.

Frederick Klauschen Frederick Klauschen studied medicine and physics in Lübeck and Hamburg, Germany, from 1995 to 2004. He received his M.D. in medical informatics from the University of Lübeck in 2005 and his habilitation in experimental pathology in 2013.

After completing a post-doctoral fellowship in biomedical computing and systems immunology at the National Institutes of Health, Bethesda, MD, USA, he moved to the Charité Universitätsmedizin Berlin in 2009 where he started his own group and his pathology residency. In Berlin, he became a Human Frontier Young Investigator and Einstein Junior Fellow and received his board certification in anatomic and surgical pathology in 2015. Since 2016 he has been a professor of molecular pathology and became deputy director of the Institute of Pathology at the Charité in 2019. He is co-chair of the Berlin Institute of Health digital medicine hub and topic leader for histopathology of the WHO-ITU focus group Artificial Intelligence for Health. He is also co-founder and chief medical adviser of the Charité/BIH-spin-off Aignostics in Berlin.

Shinichi Nakajima is a senior researcher in Berlin Big Data Center, Machine Learning Group, Technische Universität Berlin. He received the master degree on physics in 1995 from Kobe university, and worked with Nikon Corporation until September 2014 on statistical analysis, image processing, and machine learning. He received the doctoral degree on computer science in 2006 from Tokyo Institute of Technology. His research interest is in theory and applications of machine learning, in particular, Bayesian learning theory, variational inference, generative models, computer vision, explainable AI, and machine learning applications for science.

Marius Kloft Since 2017 Marius Kloft is a professor of CS and ML at TU Kaiserslautern, Germany. Previously, he was an assistant professor at HU Berlin (2014-2017) and a joint postdoctoral fellow at Courant Institute and Sloan-Kettering Cancer Center, New York. He earned his PhD at TU Berlin and UC Berkeley. MK is interested in theory and algorithms of statistical machine learning and its applications. His research covers a broad range of topics and applications, where he tries to unify theoretically proven approaches (e.g., based on learning theory) with recent advances (e.g., in deep learning and reinforcement learning). MK has been working on, e.g., multi-modal learning, anomaly detection, extreme classification, adversarial learning for computer security, and explainable AI. In 2014, MK was awarded the Google Most Influential Papers award. He has been serving as a senior AC for AAAI (2020, 2021) and AISTATS (2020, 2021), and he is an associate editor of IEEE TNNLS.

APPENDIX
SUPPLEMENTARY MATERIALS

In the following we provide the supplementary material to our paper Explaining Bayesian Neural Networks.

A. Proof of Theorem 1

For LRP-0, it holds that

$$R_W(x) = \mathcal{T}_x[f_W](x), \tag{10}$$

with $\mathcal{T}_x[f_W](x) = x \odot \nabla_x[f_W](x)$. Furthermore, the linearity

$$\tau_1 \mathcal{T}_x[f_1](x) + \tau_2 \mathcal{T}_x[f_2](x) = \mathcal{T}_x[\tau_1 f_1 + \tau_2 f_2](x)$$

holds for any $\tau_1, \tau_2 \in \mathbb{R}$ and any weakly differentiable functions f_1, f_2 except at the non-strongly-differentiable points of f_1 and f_2. We will prove, that in this case

$$\mathcal{T}_x\left[\mathbb{E}_W\left[f_W\right]\right](x) = \mathbb{E}_W\left[\mathcal{T}_x[f_W](x)\right] \tag{11}$$

holds except for measure zero points.

Let us fix x. If f_W is strongly differentiable at x for all W on the support of its posterior distribution $q(W)$, linearity of $\mathcal{T}_x$ holds and therefore Eq.(11) holds due to Lemma 1. Let us define $\mathcal{W}_x = \{W; f_W \text{ is not strongly differentiable at } x\}$, and $\mathcal{Z} = \{x; \int \delta(W \in \mathcal{W}_x)q(W)dW > 0\}$, where $\delta(\cdot)$ denotes the Dirac measure. Eq.(11) still holds for $x \in \overline{\mathcal{Z}}$, because the contribution from the set of non-differentiable models at x is zero. For any bounded distribution $q(x)$ in the input space, it holds that $\int q(x) \int \delta(W \in \mathcal{W}_x)q(W)dW\,dx = \int q(W) \int q(x)\delta(W \in \mathcal{W}_x)dx\,dW = 0$ due to the weakly differentiable assumption on f_W. This implies that $\mathcal{Z}$ is a measure zero set, which proves the claim for LRP-0.

Similarly, the gradient explanation, as well as IG, can be written as Eq.(10) with an operator $\mathcal{T}_x$ linear on all strongly-differentiable-points, and the same discussion applies to proving the claim.

B. Details of the clustering procedure

For the image classification task we employ the SpRAy algorithm as follows [34]:

1) **Relevance maps sampling**
   A collection $\{R_i\}_{i=1}^N$ of relevance maps is sampled from the posterior distribution.
2) **Preprocessing of the relevance maps.**

All relevance maps are normalized using the MinMax normalization procedure. If needed, all relevance maps should be made uniform in shape and size, for future clustering.

To speed up the clustering process and to produce more robust results we propose to use downsampling methods on the collection of samples. While the user is free to choose any dimensionality reduction method, we propose to use the Average Pooling method in order to achieve visually different strategies in different clusters.

3) **Spectral Cluster (SC) analysis on pre-processed relevance maps.**

Pre-processed relevance maps are clustered by Spectral Clustering (SC) method. The affinity matrix, which is necessary for SC method, is based on k-nearest-neighborhood relationships. More detailed, the affinity matrix $M = (m_{ij})_{i,j=1,...,N}$, measures the similarity $m_{ij} \geq 0$ between all N samples R_i and R_j of a source dataset and is constructed in the following way:

$$m_{ij} = \begin{cases} 1 & \text{if } R_i \text{ is among the k nearest neighbors of } R_j \\ 0 & \text{else} \end{cases}$$

Since this rule is asymmetric, the symmetric affinity matrix M is created by taking $m_{ij} = max(m_{ij}, m_{ji})$. Authors of the original paper highlight that similar clustering results were obtained using the Euclidean distance, with only small differences in the eigenvalue spectra.

The Laplacian L is computed from M as follows :

$$d_i = \sum_j m_{ij}.$$

$$D = diag\,[d_1, d_2, ..., d_N]\,.$$

$$L = D - M.$$

The Matrix D is a diagonal matrix, which describe the measure of connectivity of a particular sample i with D being a diagonal matrix with entries d_{ii} describing the degree (of connectivity) of a sample i [34].

4) **Identification of interesting clusters by eigengap analysis**

By performing an eigenvalue decomposition on the Laplacian L, eigenvalues $\lambda_1, \lambda_2, ..., \lambda_N$ are obtained. The number of eigenvalues $\lambda_i = 0$ identifies the number of (completely) disjoint clusters within the analyzed set of data.

The final step of SpRAy assigns cluster labels to the data points, which can then be performed using an (arbitrary) clustering method: in our work we use k-means clustering on the N eigenvectors. The number of clusters can be obtained by *eigengap* analysis [85]: it can be identified by eigenvalues close to zero as opposed to exactly zero, followed by an eigengap — rapid increase in the difference between two eigenvalues in the sequence $|\lambda_{i+1} - \lambda_i|$ [34].

C. Experimental setup

1) CMNIST experiment: For the CMNIST experiment we used a simple convolutional network similar to LeNet [80]. For the Ensemble and for the Laplace scenarios a standard architecture was used, with only a change in number of input channels adjusted to 3-dimensional RGB inputs. For the Dropout scenario, after 2 Average Pooling layers, a 2-d Dropout layer was inserted with a dropout probability set to 0.25. 2 1D Dropout layers were added in the classification part of the network, with the probability of dropout set to 0.5.

All of the networks were trained with a batch size of 32, and with a Stochastic Gradient Descent algorithm, [86] with a learning rate of 0.01 and 0.9 momentum. A learning rate scheduler was used with the number of steps set to 7 and multiplicative parameter $\gamma = 0.1$. For the Ensemble scenario 100 networks were trained for 20 epochs, and for the Laplace and Dropout the number of epochs was set to 100. For the Laplace approximation, KFAC Laplace approximation was used [87], [88], with Laplace regularization hyperparameters (additive and multiplicative) both set to 0.1.

2) Carcinoma experiment: For the Cancer experiment, we employed a standard VGG-16[60] with additional 2D Dropout layers after each MaxPooling layer, with the probability of dropout set to 0.1 and 2 1D Dropout layers in the classificator part of the network after each activation function with the probability of 0.5. The network was trained with SGD with 0.001 learning rate and 0.9 momentum. torch.optim.lr_scheduler.ReduceLROnPlateau learning rate scheduler was used with the factor of 0.1 and patience of 10.

3) Clever Hans experiment: For the Pascal VOC 2007 multi-label classification experiment, we employed a standard VGG16 network [81], and adjusted the number of output neurons from 1000 to 20, which is the number of different classes in the Pascal VOC 2007 dataset.

We resized each training image, such that the shorter axis has 224 pixels, keeping the aspect ratio unchanged. Then, we randomly cropped the longer axis and obtained square images with the size 224×224. We trained the network for 60 epochs, by minimizing the Binary Cross Entropy loss preceded with a Sigmoid layer[4]. We used the Adam optimizer with its parameters set to $\alpha = 0.0001, \beta_1 = 0.9, \beta_2 = 0.999$. Our trained VGG16 network achieves 91.6%[5] in the multi-label classification on the test set, for which center cropping with square size of 224×224 was applied, instead of random cropping.

4) Fashion MNIST experiment: For the Fashion MNIST experiment we trained a LeNet network with 2 2D Dropout layers with $p = 0.5$ added after each of the Average Polling layers in the feature extractor part of the Network, and 1 1D Dropout layer with $p = 0.5$ after the Flatten Layer. The network was trained on FashionMNIST dataset with several augmentations, such as Color Jittering, Random Affine Transformations, and Random Horizontal Flips. The batch

[4]https://pytorch.org/docs/master/generated/torch.nn.BCEWithLogitsLoss.html

[5]https://scikit-learn.org/stable/modules/generated/sklearn.metrics.accuracy_score.html

size was set to 64, the Network was trained using the Cross-Entropy loss for 50 epochs with Adam optimizer with standard parameters and a learning rate of 0.001.